Selective Formation of α-Fe(II) Sites on Fe-Zeolites through One-Pot Synthesis

Max L. Bols,[§] Julien Devos,[§] Hannah M. Rhoda, Dieter Plessers, Edward I. Solomon,[*] Robert A. Schoonheydt,[*] Bert F. Sels,[*] and Michiel Dusselier[*]

ABSTRACT: α-Fe(II) active sites in iron zeolites catalyze N_2O decomposition and form highly reactive α-O that selectively oxidizes unreactive hydrocarbons, such as methane. How these α-Fe(II) sites are formed remains unclear. Here different methods of iron introduction into zeolites are compared to derive the limiting factors of Fe speciation to α-Fe(II). Postsynthetic iron introduction procedures on small pore zeolites suffer from limited iron diffusion and dispersion leading to iron oxides. In contrast, by introducing Fe(III) in the hydrothermal synthesis mixture of the zeolite (one-pot synthesis) and the right treatment, crystalline CHA can be prepared with >1.6 wt % Fe, of which >70% is α-Fe(II). The effect of iron on the crystallization is investigated, and the intermediate Fe species are tracked using UV−vis-NIR, FT-IR, and Mössbauer spectroscopy. These data are supplemented with online mass spectrometry in each step, with reactivity tests in α-O formation and with methanol yields in stoichiometric methane activation at room temperature and pressure. We recover up to 134 μmol methanol per gram in a single cycle through H_2O/CH_3CN extraction and 183 μmol/g through steam desorption, a record yield for iron zeolites. A general scheme is proposed for iron speciation in zeolites through the steps of drying, calcination, and activation. The formation of two cohorts of α-Fe(II) is discovered, one before and one after high temperature activation. We propose the latter cohort depends on the reshuffling of aluminum in the zeolite lattice to accommodate thermodynamically favored α-Fe(II).

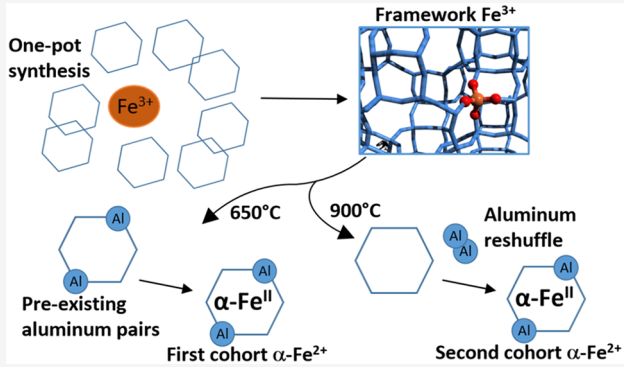

1. INTRODUCTION

Zeolites are composed of tetrahedrally coordinated oxygen-bridged Si(IV) and Al(III) atoms that make up a three-dimensional crystalline framework with ordered micropores. These framework Si(IV) and Al(III) are also referred to as T atoms. For every Al(III) T atom, the lattice carries a negative charge that must be balanced by exchangeable cations. Zeolites exchanged with cationic iron are useful redox catalysts and attract attention for their stabilization of the α-Fe(II)/α-O sites.[1−3] These are well-known as the active sites for room temperature partial oxidation of methane to methanol and benzene to phenol and are likely also involved in selective catalytic reduction (SCR) of NO_X and catalytic N_2O decomposition.[4−8] On the Fe-*BEA zeolite, the α-Fe(II)/α-O active sites are formed in six membered ring (6MR) motifs of the zeolite framework with two Al(III) T atoms (Al_{FW}) at opposite sides of the 6MR.[9] How these α-Fe(II) sites are formed from their precursors remains unclear. Understanding this process may allow the preparation of Fe-zeolites with high α-Fe(II) density while simultaneously avoiding other types of iron species. This would facilitate mechanistic catalytic research and improve active site purity, leading to better catalysts. In the context of methane partial oxidation, a higher α-Fe(II) site density directly improves the single turnover methanol yield in the typically stoichiometric reaction cycle, and lower concentrations of other iron may avoid over-oxidation improving methanol selectivity. Currently obtained methanol yields per cycle with iron zeolites reach 70 μmol/g (at 2 wt % Fe), too low for any reasonable application.[10] Recently we showed that α-Fe(II) sites can also be formed on iron exchanged chabazite (Fe−CHA) where they occupy similar exchange sites in the double six ring motifs (d6r) of the framework, requiring a similar configuration of two Al(III) T atoms (Figure 1).[11] Given CHA is particularly rich in 6MRs, it can, in theory, host a high density of α-Fe(II) sites.[11] From the density of d6r units in CHA and taking into account Löwenstein's rule (implying at most one α-Fe(II) per d6r),

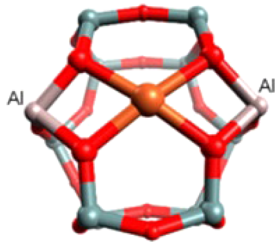

Figure 1. α-Fe(II) site in the CHA d6r. Adapted with permission from ref 11. Copyright 2018 American Chemical Society.

Fe−CHA with Si/Al = 5 can theoretically support 7.9 wt % α-Fe(II), corresponding to 1390 μmol Fe/g and thus as many methane activating sites. Nevertheless, single-site α-Fe(II) has been successfully prepared only up to ∼0.3 wt % Fe by an impregnation of the zeolite with $Fe(acac)_3$ in toluene.[11,12]

CHA is classified as a small-pore zeolite, in which the crystalline framework is built up of rings composed of eight T atoms or less (i.e., "eight-membered rings" or smaller, ≤8MR). Small-pore iron zeolites are known to have attractive properties for catalysis.[13] In selective catalytic reduction (SCR), the small pores prevent the clustering of Cu and Fe active sites and aluminum.[14−16] In methane activation with α-O, the restricted windows in CHA enable catalytic turnover.[17] However, the restricted pore hinders the dispersion of iron during catalyst preparation and favors the formation of inactive Fe oxide clusters.[11,18] Here we introduce iron during hydrothermal synthesis ("one-pot synthesis"). Such preparations yield active Fe zeolite catalysts for numerous reactions, but the active sites are generally unknown.[19] The one-pot method suppresses cluster formation and eliminates the need for $Fe(acac)_3$ and toluene. It enables high-purity α-Fe(II) in Fe−CHA with Si/Al ∼ 12 at high Fe loadings. Over 70% of iron forms α-Fe(II), even at substantially elevated Fe loadings of 1.6 wt %, corresponding to Fe/Al = 0.23 or ∼288 μmol Fe/g. The method thus enables the use of ≥31% of available aluminum to stabilize α-Fe(II). Based on spectroscopic and mass spectrometric data, we explain the postsynthesis steps in Fe speciation from Fe(III) in the zeolite framework to α-Fe(II) and propose a model in which two cohorts of α-Fe(II) are formed. A first fraction is formed after template removal, dehydration, and autoreduction below 650 °C. The second fraction is formed after Al(III) mobilization at ∼850 °C. The materials are tested for the formation of α-O from N_2O at 180 °C and the room temperature reaction of α-O with CH_4 to give extractable methanol. The stoichiometric methanol yield is augmented to 134 μmol/g from aqueous liquid extraction, or 183 μmol/g from online steam desorption, double the current record for Fe-zeolites and on par with high loading, multisite Cu-zeolites reacted at 200 °C.[10,20,21]

2. EXPERIMENTAL SECTION

2.1. Material Synthesis: Iron Introduction. *2.1.1. Postsynthetic Impregnation.* The postsynthetic iron introductions are based on the introduction method used in ref 11. Variations on this procedure are explained in the Supporting Information (section S1 and Tables S1 and S2). The zeolites with postsynthesis, iron introduction zeolites are labeled as follows ,"$framework(iron\ introduction\ method)_{Fe\ concentration}$". The examined frameworks are CHA, FAU, FER, and *BEA. The *iron introduction method* between brackets indicates water or toluene as solvent by, respectively, "W' or 'T" and the use of $Fe(acac)_3$, $Fe(NO_3)_3$, or iron oxide as Fe sources by, respectively, "A", "N", or "O" (see also the Supporting Information section S1.2 and Tables S1 and S2). The iron concentration in the solid material in the subscript is in μmol/g.

2.1.2. Hydrothermal CHA Synthesis. All CHA crystallizations use *N,N,N*-trimethyl-1-adamantammonium hydroxide (TMAdaOH, obtained from Sachem) as organic structure directing agent (OSDA). Synthesis details are explained in sections S1.1 (without Fe) or S1.3 (one-pot Fe−CHA). A one-pot Fe−CHA preparation is labeled "$synthesis\ type(iron\ source)_{Fe\ concentration}$". The "synthesis type" is either "IZC" or "Am", the used iron sources $Fe(acac)_3$, $^{57}Fe(acac)_3$, $Fe(NO_3)_3$, and Fe_3O_4 are labeled, respectively, "A", "^{57}A", "N", and "O", and the iron concentration in the subscript is in μmol/g for the solid material. A dagger ("†") superscript indicates impure CHA phase or no CHA at all. The "IZC" synthesis type contains syntheses starting from FAU (US-Y, Zeolyst CBV720, Si/Al = ∼13) as Si and Al source, while "Am" type syntheses start from amorphous Si (LUDOX HS-40, Sigma-Aldrich) and Al sources ($Al(OH)_3$, Sigma-Aldrich). Typical stoichiometric batch compositions are $1Si{:}0.067Al{:}0.36TMAda^{+}{:}0.017Fe^{3+}{:}0.36OH^{-}{:}15.5H_2O$. All syntheses are summarized in Table S3. For some supporting experiments a deviating "synthesis type" was used as explained in section S1.3.

2.2. Gas Flow Treatments. Zeolite samples were pelletized to 250−500 μm and loaded into a quartz reactor fitted with a window for *in situ* DRS-UV−vis-NIR and a pyrex side arm for *in situ* Mössbauer measurements. A standard treatment procedure after calcination consists of an activation step in a 20 mL/min flow of dry He at 900 °C for 5 h, treatment in 35% N_2O/He atmosphere for 25 min at 180 °C, and a 10 min treatment in 30 mL/min CH_4 flow at room temperature. Steam desorption at room temperature was performed by passing a 35 mL/min He stream through a bubbler with water and then through the sample at room temperature. A typical methanol desorption run took 25 h. All flows were controlled with mass flow controllers (Brooks Instrument 0154). Flows are given for STP conditions.

2.3. Extraction and GC Analysis. To quantify methanol yields, a known mass (∼0.2 g) of dry sample was transferred into a 7 mL screw lid vial with 1 mL of distilled water, 1 mL of acetonitrile, and a stirring rod. The mixture was allowed to stir for 24 h (800 rpm) at room temperature and then centrifuged. The solution was analyzed on an Agilent 6850 gas chromatograph fitted with an HP1 column and a flame ionization detector (GC-FID).

2.4. Characterization. *2.4.1. XRD.* The structure and crystallinity of the zeolites were confirmed by X-ray powder diffraction (P-XRD) on a high-throughput STOE STADI P Combi diffractometer in transmission mode with focusing Ge(111) monochromatic X-ray inlet beams (λ = 1.5406 Å, Cu Kα source). Crystallinity for CHA was calculated relative to a reference sample as the sum of peak areas at 16.2°, 20.9°, and 31.1°.

2.4.2. N_2 Physisorption. Porosity was measured by nitrogen physisorption (Tristar II 3020, Micromeritics) at 77 K on calcined and dried samples (6 h at 300 °C). The relative nitrogen pressure was varied between 0.01 and 0.99 (p/p_0). The t-plot method (Harkins and Jura) on the adsorption branch was used to determine micropore volumes.

2.4.3. NMR. ^{27}Al and ^{29}Si solid state nuclear magnetic resonance (SS NMR) were measured on a Bruker 500 MHz NMR spectrometer and using a Bruker 4 mm MAS probe. ^{29}Si MAS NMR was recorded after a 4-μs 90 deg pulse under a sample spinning rate of 8 kHz and referenced externally to tetramethylsilane (TMS). Solid-state ^{27}Al MAS NMR was measured at a spinning rate of 13 kHz and referenced to a 1 M aqueous solution of aluminum nitrate.

2.4.4. Element Analysis. The elemental analysis was performed using an inductively coupled plasma-atomic emission spectrometer (ICP-AES, PerkinElmer Optima 3300 DV) with signals for Fe, Al, and Si at 228.6, 238.2, and 251.6 nm, respectively. Before ICP-AES, the samples were dissolved using HF and aqua regia, neutralized using boric acid, and diluted using 0.42 M HNO_3 in water.

2.4.5. Mass Spectrometry. Part of the gas outflow from the quartz reactor was channeled via a flow split into a capillary tube connected to an Omnistar Pfeiffer Vacuum GSD 30102 quadrupolar mass spectrometer (QMS). For methanol quantification, the m/z = 31

Table 1. Material Properties and Methanol Yields for a Selection of the Samples in This Study[a]

preparation[b]	lattice	Si/Al[d]	wt % Fe	Fe/Al[d]	Fe retention (%)[e]	μmol Fe/g	methanol (μmol/g)[f]	methanol/Fe[d]	methanol/Al[d]
				Postsynthetic Fe(III)					
$CHA(TA)_{57}$	CHA	10	0.32	0.04	19	57	15	0.26	0.010
$CHA(TA\text{-}105\ °C)_{124}$	CHA	12	0.69	0.1	42	124	42	0.34	0.034
$CHA(WA)_{92}$	CHA	10	0.52	0.06	31	92	32	0.35	0.021
$Na{-}CHA(WN)_{136}$[g]	CHA*[h]	9	0.76	0.09	45	136	48	0.35	0.032
$FAU(TA)_{221}$	FAU	15	1.23	0.22	35	221	3	0.01	0.002
$BEA(TA)_{193}$	BEA	13	1.08	0.16	91	193	30	0.16	0.026
				One-Pot Fe(III)					
$IZC(A)_{315}$	CHA	13	1.76	0.27	90	315	105	0.33	0.089
$FAU(TA)_{349}\text{-}IZC_{259}$[c]	CHA	13	1.45	0.22	74	259	76	0.29	0.064
$IZC(^{57}A)_{288}$	CHA	12	1.61	0.23	100	288	105	0.37	0.085
$IZC(N)_{274}$	CHA	13	1.53	0.23	87	274	128	0.47	0.108
$IZC(A)_{490}$	CHA	13	2.74	0.43	84	490	134	0.27	0.116

[a]A full overview is given in Tables S2–S4. [b]The sample naming code is given in the section 2.1. [c]Hydrothermal synthesis starting from postsynthesis exchanged $FAU(TA)_{349}$. [d]Molar ratios. [e]As ratio of Fe in the recovered solid product/Fe added in the preparation procedure. [f]From liquid extraction and GC analysis, see section 2.3. [g]Sample starting from Na-form CHA instead of H-form CHA. [h]This sample was prepared starting from a different H–CHA, designated CHA*; details in section S1.1.

signal was referenced to the $m/z = 4$ signal as an internal standard and then calibrated to a series of desorption of known amounts of methanol from a zeolite.

2.4.6. Diffuse Reflectance UV–vis-NIR Spectroscopy. Diffuse reflectance spectroscopy in the UV–vis-NIR energy range (DRS-UV–vis-NIR) was performed with a Varian Cary 5000 UV–vis-NIR spectrophotometer equipped with the internal DRA 2500 accessory at room temperature against a Halon white reflectance standard in the 4000–50000 cm^{-1} energy range. All treatments before UV–vis-NIR spectroscopy were performed in a quartz U-tube/flow cell, equipped with a window for *in situ* measurements.

2.4.7. Mossbauer Spectroscopy. ^{57}Fe Mössbauer spectra were recorded at liquid helium temperature or at room temperature with a See Co. W302 resonant gamma ray spectrometer in horizontal geometry at room temperature with a zero external field using a 1.85 GBq source (Be window, Rh matrix). Data were collected from samples enriched with 50% ^{57}Fe. Isomer shifts are given relative to α-iron foil at room temperature. Spectra were collected with 1024 points and summed up to 512 points before analyzing. Spectra were fit to Lorentzian doublets and hyperfine-split multiplets using the Vinda software package for Microsoft Excel. The spin Hamiltonian model, SPINHAM, was used to fit the hyperfine features with an extremely small magnetic field. Samples were measured in sealed pyrex vials ensuring *in situ* measurement conditions.

2.4.8. Fourier Transform Infrared (FT-IR) Spectroscopy. Fourier transform infrared (FT-IR) spectroscopy was performed using a Nicolet 6700 spectrometer equipped with a deuterated triglycine sulfate (DTGS) detector. Prior to analysis, samples were pressed (10^7 Pa) into precisely weighed self-supported wafers with a similar disc mass density (9.1–9.7 mg/cm^2) and degassed in situ at 400 °C (5 °C/min heating rate) for 1 h under vacuum (<1 mbar). After degassing, the cell was cooled to 150 °C and a spectrum of the material was recorded with an accumulation of 128 scans at a resolution of 2 cm^{-1}. The differential spectra were normalized to a constant disc mass.

2.5. DFT Modeling. DFT models were generated from crystallographic coordinates of the CHA zeolite. Structures were capped with hydrides 1.42 Å away from the Si atoms. Spin-unrestricted DFT calculations were performed with Gaussian 16[22] using the B3LYP functional with D3 empirical dispersion correction from Grimme.[23] For the optimization, the 6-311G* basis set was used for Fe and for atoms directly coordinated to Fe and the 6-31G* basis set was used for all other atoms. Mössbauer quadrupole splittings were calculated using the B3LYP functional, with the TZVP basis set on Fe and coordinating atoms and the 6-31G* basis set on all other atoms. Isomer shifts were calculated with the ORCA computational package (version 303)[24] using the B3LYP functional. The CP(PPP) basis set[25] was used on the Fe atom and the 6-311G* basis set was used on the coordinating atoms. The 6-31G* basis set was used on all other atoms for these calculations. A calibration curve was generated by relating the DFT-calculated electron densities at the iron nucleus to the experimental isomer shifts for a test set of 23 structurally defined Fe complexes. The isomer shift values were then estimated from the value calculated for each cluster model. Small models of the CHA 6MR were evaluated with a proton far away or close to the Fe and with either one or two water molecules added.

3. RESULTS AND ANALYSIS

3.1. Postsynthetic Fe Introduction. A classical iron introduction method is postsynthetic diffusion impregnation of $Fe(acac)_3$ in toluene onto a zeolite in proton form. In previous work, we impregnated H–CHA with Si/Al = 12 to contain 0.47 wt % Fe, equivalent to Fe/Al = 0.048 or 85 μmol Fe/g. The sample was calcined in air at 580 °C and treated in He at 900 °C. About 50% of Fe irreversibly formed iron oxide clusters. The other half formed α-Fe(II).[11] Only 32% of the iron from $Fe(acac)_3$ was retained in the final material.[11] $CHA(TA)_{57}$ in Table 1 represents the classical preparation method in this study with 0.32 wt % Fe. Other recipes for postcrystallization Fe introduction with different Fe salts and solvents were attempted, and some improvement in Fe retention was achieved by increasing the iron introduction temperature, by changing the solvent to water, and by starting from Na^+- instead of H^+-exchanged zeolite (Table 1). The formation of Fe oxide clusters could be somewhat suppressed but not avoided entirely by these methods (see also section 3.5). Additional high temperature treatments in O_2 or H_2 reversibly oxidized or reduced spectator iron but did not affect the iron oxide clusters (Supporting Information section S4), indicating the irreversibility of cluster formation upon calcination. $Fe(acac)_3$ impregnation at 105 °C instead of room temperature increased iron retention and decreased clusters (sample $CHA(TA\text{-}105\ °C)_{124}$). This suggests a kinetic diffusion barrier hinders dispersion of Fe through the small-pore system of CHA. This is confirmed by comparing small-pore CHA to large-pore *BEA where Fe retention was >80%. On FAU where access to the d6r cages is blocked by

unpassable 6MR windows, Fe retention was 35% but hardly any α-Fe(II) sites were formed.

3.2. One-Pot Preparation of Fe−CHA. In one-pot methods, diffusion into the pore system is not required, and one-pot methods yield better catalysts for NH_3−SCR of NO_X above 450 °C.[18] However, the Fe species after calcination and especially after high temperature autoreduction remain ill-characterized.[19,26−29] One-pot Fe−CHA was prepared here both from amorphous sources of Si and Al and through interzeolite conversion (IZC) from FAU. Several Fe sources were tested. High iron retentions (84−100%) were observed for all hydrothermal Fe preparations except when using Fe_3O_4 ($IZC(O)_{180}$) (Table 1 and Table S3), confirming that one-pot methods alleviate the postsynthetic low loading issues. Within the scope of this work, and the techniques we applied, no significant differences could be noted between the IZC preparations and those from amorphous Si and Al (Supporting Information section S5). P-XRD, N_2 physisorption, and ^{27}Al SS NMR measurements only deviated from crystalline CHA zeolite when excessively high Fe loadings were used (Figures S1−S3 and S6). The following sections elaborate on Fe loading, retention, and speciation and on Fe−CHA crystallization and stability. Additional information on the one-pot syntheses can be found in the Supporting Information section S2.

3.3. Crystallization and Thermal Stability. The incorporation of multivalent cations is known to result in higher thermal stability.[15,30−34] After 5 h at 900 °C in helium, our H−CHA parent material without Fe lost 50% of its crystallinity, but on $CHA(TA)_{57}$ with Fe/Al = 0.04 only 31% crystallinity was lost (Figure S4). The thermal stability improved further for one-pot syntheses with higher Fe loadings. $IZC(N)_{290}$ lost 32% of crystallinity, whereas $Am\text{-}(A)_{542}$ lost only 17% (Figure S5). The solid phase yield from the one-pot preparations with Si/Al ∼ 12 was 0.94 ± 0.07% (error intervals indicate standard deviation). This is significantly higher than the 0.74 ± 0.01% for hydrothermal syntheses without Fe (Table S3) and could be related to Fe lowering Si solubility (section S2.3).[35] At still higher Fe loadings (>800 μmol/g; Fe/Al > 0.7), the yield of CHA decreased (Figure S6). At these high iron loadings, using $Fe(acac)_3$ as an iron source yielded more crystalline CHA than using $Fe(NO_3)_3$ (Figure S6). In $IZC(N)_{1398}$ with Fe/Al= 1.2, no CHA reflections were observed by P-XRD (Figure S6).

3.4. Spectroscopic Tracking of Iron. The one-pot method enabled high Fe retention and loading on crystalline CHA. We will now spectroscopically track the iron speciation on $IZC(^{57}A)_{288}$, enriched with ^{57}Fe isotope (see also section S6). The standard postcrystallization treatment to prepare α-Fe(II) consists of a calcination step at 550 °C in air, followed by either steaming at 650 °C or heating at 900 °C in an inert atmosphere.[36] This produced nearly single site α-Fe(II) at low Fe loadings, which is replicated in this study.[11,12] Intermittent room temperature UV−vis-NIR and 6 K Mössbauer spectra after IZC, drying, calcination, and autoreduction are shown in Figures 2 and 3. Before calcination, the Mössbauer spectrum showed an IS = 0.33 mm/s; |QS| = 0.02 mm/s feature with paramagnetic relaxation, characteristic of isolated high-spin tetrahedral Fe^{3+} incorporated in the zeolite framework ($Fe(III)_{FW}$).[37−39] No other forms of iron were observed. In UV−vis-NIR DR, the weak spin forbidden d−d transitions at 20830, 22830, 24210, and 26750 cm^{-1} are observed as well as

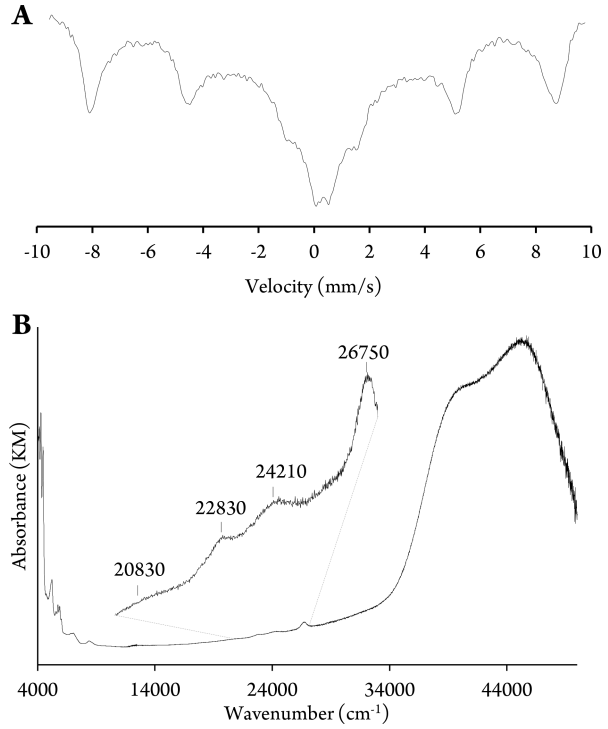

Figure 2. Spectroscopy on the $IZC(^{57}A)_{288}$ sample before calcination: (A) Mössbauer spectrum measured at 6 K and (B) UV−vis-NIR spectrum measured at room temperature.

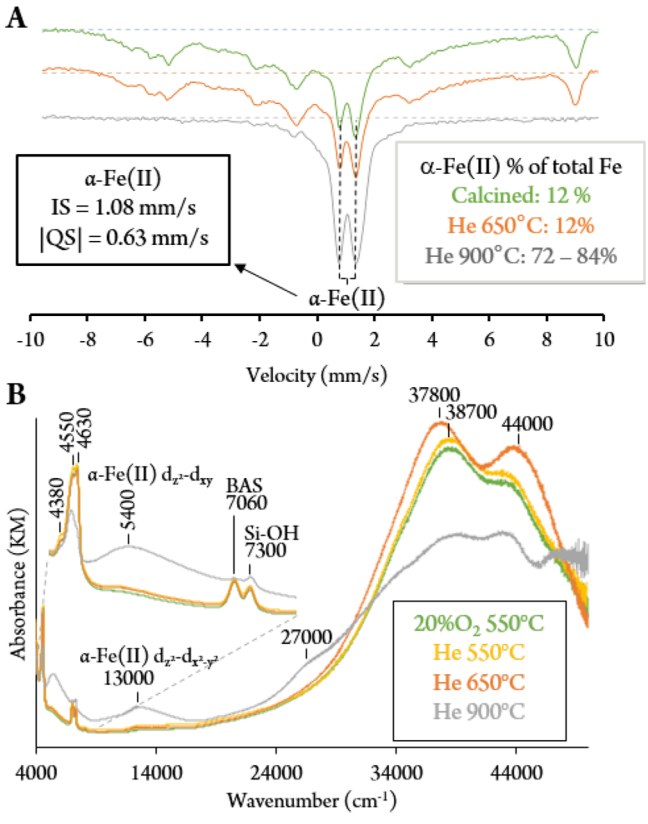

Figure 3. (A) *In situ* Mössbauer spectra measured at 6 K and (B) *in situ* UV−vis-NIR spectra measured at room temperature of the $IZC(^{57}A)_{288}$ sample along the calcination and He 900 °C steps. For deconvolution of the Mössbauer spectra, see the Supporting Information section S7.

the two strong CT bands between 30000 and 50000 cm^{-1} of $Fe(III)_{FW}$.[40−43]

Upon calcination in 20% O_2/He at 580 °C (~dry air), organic template and chemisorbed water were fully removed and the overtones of the O−H stretches of Brönsted acid sites (BAS) at 7060 cm^{-1} and silanol at 7300 cm^{-1} became (partially) resolvable (Supporting Information section S6 and Figures S14 and S15). The fundamental OH stretches of silanol and BAS appeared on the FT-IR spectra (Figures S20 and S23). The electronic transitions and Mössbauer features of $Fe(III)_{FW}$ disappeared, and the Mössbauer spectrum became more complex and asymmetric (Figure 3A). The Mössbauer spectrum contains a doublet with IS = 1.10 mm/s and |QS| = 0.67 mm/s, attributed to α-Fe(II).[11] We can quantify this doublet and estimate its contribution at 12 ± 5% of all iron (Supporting Information section S7). Subtracting the α-Fe(II) contribution from the spectrum leaves a combination of a hyperfine split contribution with E/D = 0.3; D = −0.8 cm^{-1}; IS = 0.28 mm/s; QS = +1.9 mm/s and a doublet with the same QS and IS values. In the Supporting Information section S7, we show that the doublet and the hyperfine component derive from a single isolated Fe(III) species as the hyperfine splitting collapses into the doublet at room temperature. The UV−vis-NIR spectra (Figure 3B) retained two CT bands between 30000 and 50000 cm^{-1}, somewhat red-shifted from the CT bands in the precalcination spectrum. In the absence of d−d bands between 20000 and 26500 cm^{-1}, such CT absorbance features have been assigned to octahedrally coordinated Fe(III), but that assignment is not necessarily exclusive.[44]

After calcination in 20% O_2/He, no further changes in Mössbauer or UV−vis-NIR absorption occurred in dry helium flow up to 650 °C. With further heating to 900 °C, however, O_2 desorbed from the sample indicating autoreduction of Fe(III) to Fe(II) (section S6). Thus, $Fe(III)_{FW}$ with IS = 0.33 mm/s and QS = 0.02 mm/s converts into the Fe(III) site with IS = 0.28 mm/s and QS = +1.9 mm/s, which further converts to α-Fe(II). Mössbauer spectroscopy provides insight into the structural changes required to set $Fe(III)_{FW}$ free from the lattice and then reduce it to form α-Fe(II). Using DFT, a model tetrahedral $Fe(III)_{FW}$ site, with the proton required for charge balance placed distant from the Fe(III), was created and geometry optimized (Figure 4A). This gave Mössbauer parameters IS = 0.15 mm/s and a reasonably small QS = +0.92 mm/s. This QS predictably overestimates the experimental QS value due to the small model size, which results in a geometry for the intralattice Fe(III) model that deviates excessively from tetrahedral.

Building on the Fe intralattice model (Figure 4A), a series of small models was then evaluated with either a proton close to the intralattice Fe(III) site or one or two water molecules added to the model (see the Supporting Information section S11). This is similar to some DFT studies on the formation of extra-framework aluminum,[45−47] but for Fe similar studies are lacking. Mössbauer parameters for the optimized structures and their energies relative to appropriate references were generated. Only the model with the proton located on a bridging O atom next to the Fe(III) reproduced the small change in the experimental IS between the precalcined and the calcined samples (Figure 4B). This model also reproduced the large increase in QS and its positive value (QS = +2.7 mm/s; low asymmetry parameter). While the initial separation of the proton from the lattice charge introduced by Fe(III) substitution simply reflects the charge compensating cation,

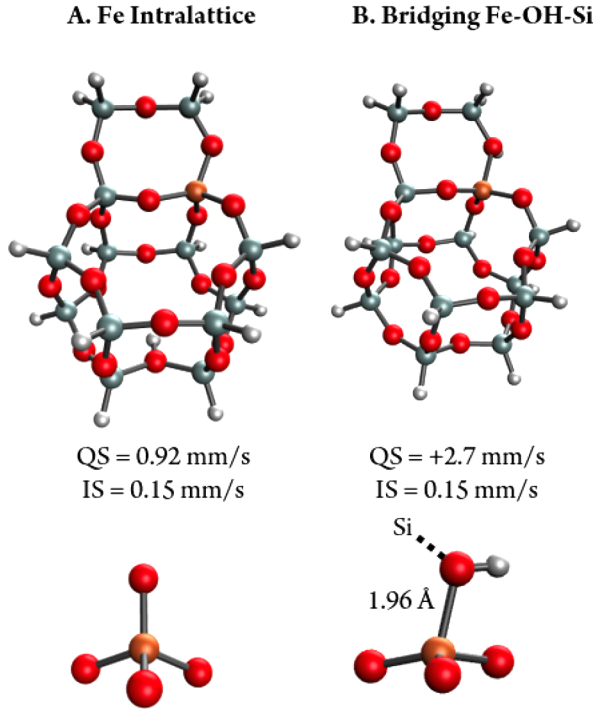

Figure 4. DFT optimized structures, the Mössbauer parameters, and the ligand coordination around the Fe(III) in (A) the Fe intralattice with distant proton and (B) bridging Fe−OH−Si with an adjacent proton.

we use these models to show that $Fe(III)_{FW}$ starts from a near-perfect tetrahedral coordination and after calcination becomes strongly distorted due to perturbation of an adjacent bridging oxo. This can labilize the Fe(III) for autoreduction. Figure S26 evaluates further intermediates in the hydrolysis of the Fe−O_{FW} bonds. These DFT models do not reproduce the experimental Mössbauer changes relative to the framework Fe(III), or they are not energetically attainable. Additionally, DFT models where Fe(III) has fully left the lattice and takes an ion exchange position next to the framework Al as $[Fe(III)(OH)_2]^+$ or $[Fe(III)O]^+$ were evaluated (Figure S25) but did not result in Mossbauer parameters similar to the experiment Mössbauer data.

Thus, the DFT calculations, correlated to the experimental Mössbauer data, suggest that during the calcination process, the $Fe(III)_{FW}$ does not directly transform into α-Fe(II) and instead loses its tetrahedral symmetry and is labilized to detach from the lattice. The most fitting DFT model suggests that in this intermediate, a bridging Fe(III)−O−Si is protonated to form an Fe(III)−OH−Si site with distinctive IS Mössbauer parameters. However, the mechanism for this iron reduction and mobility requires further evaluation.

After treatment at 900 °C, the remaining Fe(III) definitely detaches from the lattice to form more α-Fe(II). The α-Fe(II) fraction rose to ~72% of iron (Figure 3A), which is remarkable for such high Fe-content of $IZC(^{57}A)_{288}$. The full deconvolution is shown in Figure S16 and includes a sextet from irreversibly formed Fe(III) oxide clusters (~7%), the ferric precursor (IS = 0.28 mm/s, |QS| = 1.9 mm/s; ~9%), and an Fe(II) spectator (IS = 1.2 mm/s, |QS|=2.3 mm/s; ~12%). The Fe(II) spectator likely derives from α-Fe(II) with an axial ligand impurity that entered during sample preparation (e.g., H_2O, see the Supporting Information section S7).[12] We can

therefore say the sample had 72−84% of its Fe content in α-Fe(II). The UV−vis-NIR spectrum (Figure 3B) after 900 °C treatment showed a large increase in the characteristic α-Fe(II) absorption bands at 13000 and 5400 cm^{-1}[111] and some increased absorption at 27000 cm^{-1} from Fe(III) clusters.[19] Absorption features at 38700 and ∼44800 cm^{-1} from isolated Fe(III) or small clusters decreased. Also the combination bands at 4300−4700 cm^{-1} and the overtones at 7000−7400 cm^{-1} of the silanol and BAS OH stretches decreased in the UV−vis NIR spectrum, as did the corresponding fundamental O−H stretches in FT-IR (see section S8 and Figures S20 and S22). Silanols dehydrate to form Si−O−Si bridges above 800 °C, and Brønsted acid sites are lost as H^+ is replaced by α-Fe^{2+} cations. Fe(II) now fully compensates lattice charge $(AlO_4^-)_{FW}$ instead of extra-framework oxygen and/or hydroxyl ligands (O_{EF}^{2-} and OH^-). Both of these processes release H_2O, also detected by MS (Supporting Information section S6). A small feature at ∼3700 cm^{-1} that increased in the FT-IR data may be an OH stretch related to extra-framework aluminum hydroxyl, indicating aluminum removal from the framework.

The spectroscopic data show that a first cohort (12% of iron) of α-Fe(II) was easily formed, requiring only iron introduction and dry calcination. A second cohort was only formed at 800−900 °C when further autoreduction occurred. α-Fe(II) can coordinate axial ligands, but these are easily removed by heating (∼700 °C) (section S4). To find out what blocks the conversion of the second cohort of Fe(III) into α-Fe(II), we took a calcined sample and treated it in H_2 at 580 °C to force reduction of its Fe(III) to Fe(II). We then compared the stoichiometric yields of methanol and found the H_2 step was ineffective at increasing α-Fe(II). After the 580 °C hydrogenation step, 58.5 μmol of methanol per gram could be recovered, compared to 38.5 μmol/g when replacing H_2 by He. This is an increase but only a limited one compared to the increase to 115.5 μmol/g achieved with helium at 900 °C. The modest increase to 58.5 μmol/g is likely due to less overoxidation of methanol by oxidized spectator iron. Therefore, the removal of oxygen is unlikely to be the bottleneck in forming the second α-Fe(II) cohort. Hence the irreversible change brought about at 800−900 °C must be another phenomenon that enables further reduction of Fe(III).

3.5. Fe(III) Transformation to α-Fe(II). The conversion of >72% of iron to α-Fe(II) on the IZC(^{57}A)$_{288}$ preparation could not be achieved when high loadings of Fe were introduced postsynthetically. In addition to the α-Fe(II) features at 5400 and 13000 cm^{-1}, absorption bands at 18000 cm^{-1} and ∼12000 cm^{-1} are seen in their UV−vis-NIR spectra after He at 900 °C (Figure 5, bottom three spectra). The latter two are common absorption features of Fe oxide clusters.[11,48,49] The high-loading postsynthesis Fe-introduced samples also gave broad absorption bands at 4000−9000 cm^{-1}, broadening the absorption feature at 5400 cm^{-1}. Bands in this region can be ascribed to spin-allowed d−d transitions of Fe(II), and they are reversibly oxidized by O_2 (Figure S10). Probably these are small clusters and isolated Fe(II) that occupy other exchange sites than α-Fe(II).

UV−vis-NIR spectra of the other one-pot methods with similar Fe loadings to IZC(^{57}A)$_{288}$ were similar, with intense α-Fe(II) features (Figure 5, second to fourth spectra from the top). For one-pot reparations, some exceptions were noted though (see section S10). For crystalline CHA samples with over 400 μmol Fe/g, the α-Fe(II) features are no longer clearly resolvable (top spectrum in Figure 5 and Figure S12). These

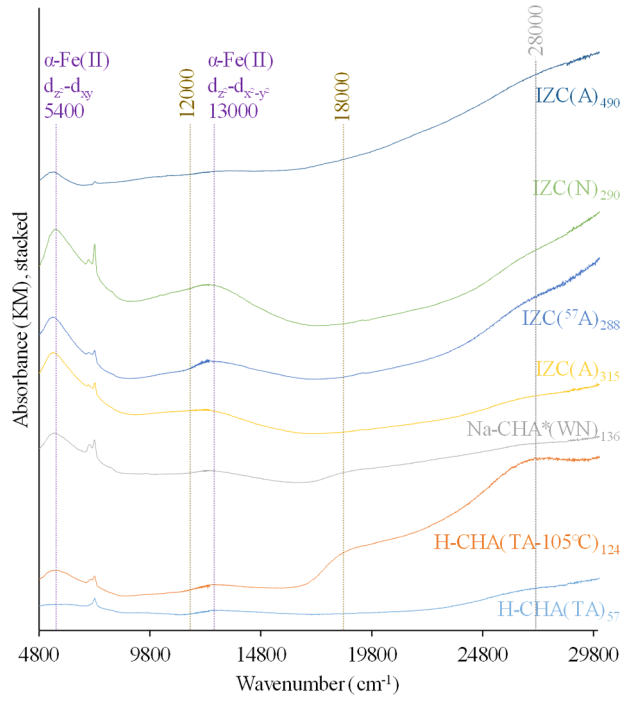

Figure 5. *In situ* UV−vis-NIR spectra after He 900 °C of different one-pot and postsynthesis samples. Full range spectra and those of other samples in the study are found in Figure S12.

samples do still activate N_2O and CH_4 to produce methanol (Figure 6 and Figure S7), and we show in the next section that

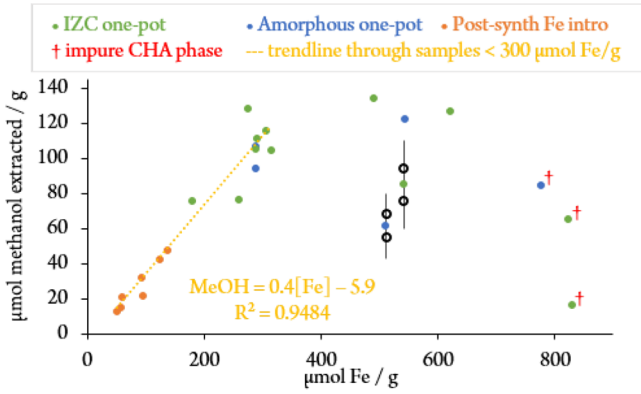

Figure 6. Plot of methanol extracted versus iron loading for the Fe−CHA samples in this study; the methanol/iron versus iron loading plot and plots labeled with sample names are found in Figure S7. For two samples, the average (colored sphere) of two measurements (open spheres) is shown along with the 95% confidence interval.

α-Fe(II) sites are still responsible for their reactivity. However, the methanol/Fe ratio is lower than for the lower Fe loading samples (Table 1), and the α-Fe(II) absorption features are obscured by surrounding features from a heterogeneous mix of different iron species.

3.6. α-O Formation and Methane Activation. After forming α-Fe(II) through calcination and He at 900 °C, the α-O reactive intermediate was formed by heating the α-Fe(II) sample in a 35% N_2O/He atmosphere at 180 °C for 25 min. This procedure converted ∼80% of α-Fe(II) to α-O on low loading samples (section S3 and Figure S9). After the N_2O reaction, the sample is cooled to room temperature and the

atmosphere is replaced by 100% CH_4. Intermittent UV−vis-NIR spectra were measured between the reaction steps. After methane reaction, methanol was recovered and quantified through liquid extraction with a water/acetonitrile mixture. This reaction sequence and product quantification were performed for most samples included in this study. The methanol yields and methanol/Fe ratios are tabulated in Table 1 and Tables S2 and S4 and the data are plotted against the Fe loading in Figure 6 and Figure S7. In addition, a series of online steam desorptions were done on a one-pot sample with 1.86 wt % Fe. This resulted in a maximum stoichiometric methanol yield of 183 μmol/g (Figure S27).

The methanol yields can be related to α-Fe(II) sites and their spectroscopic features, although three points must be considered. (1) We assume that the room temperature reaction of methane occurs exclusively on α-O sites. (2) α-Fe(II) is not fully converted to α-O, and the conversion of α-Fe(II) and the selectivity to α-O in N_2O reaction depends on the reaction conditions (controlled variable) but also on the sample's iron loading and speciation (independent variable). (3) The number of reacted α-O is not expected to equal the extracted methanol,[50] and the ratio of the two likely depends on the sample's iron loading and speciation. We discuss these three points at length in the Supporting Information section S3 and find that assumption 1 is reasonable, but points 2 and 3 can lead to variance in the ratio of extracted methanol to α-Fe(II) concentration. We therefore expect not necessarily a linear trend but still a positive correlation of methanol yield with α-Fe(II). For this reason, only general trends and not individual changes in the preparation method should be considered in the evaluation of the methanol yields from the different samples.

As already anticipated from their spectroscopic data, the one-pot preparations yielded more methanol. From $IZC(A)_{490}$, 134 μmol/g was extracted, compared to 48 μmol methanol/g from the best performing postsynthesis Fe-introduction zeolite in this work. With IZC, double the currently published yields after stoichiometric N_2O/CH_4 reaction on Fe-zeolites was achieved.[11,12,36] The highest molar methanol/Fe ratio in this study was 0.47 from $IZC(N)_{274}$ with an extraction yield of 128 μmol/g. From the $IZC(^{57}A)_{288}$ preparation, where >72% α-Fe(II) was measured from Mössbauer spectroscopy, 105 μmol methanol/g was recovered, corresponding to methanol/Fe = 0.38 or methanol/α-Fe(II) = 0.52. Beyond loadings of 300 μmol Fe/g, the methanol yield plateaus, indicating that further improvement in α-Fe(II) concentration is limited (Figure 6). The yield declines above 600 μmol Fe/g. This agrees with the results from UV−vis-NIR spectroscopy in Figure 5 indicating declining Fe(III) transformation to α-Fe(II). $IZC(A)_{490}$ shows only limited α-Fe(II) features at 5400 and 13000 cm^{-1}. CHA-crystallinity is also reduced at high Fe loadings (samples included in the Supporting Information labeled with a † superscript).

4. DISCUSSION

4.1. Quantification of α-Fe(II). The study of Fe-zeolite catalysts has been obstructed by the complex mixture of iron species derived from the chemistry of Fe in solution and on the zeolite surface and by ambiguity in the assignment of spectroscopic features.[7,44] Over the past 5 years, the structure and spectroscopy of the α-Fe(II) active site have been described,[9,11,12] and we can now reinterpret findings from past Fe zeolite studies on α-Fe(II) formation to arrive at a consistent model. In doing so, we will maintain the original definition of α-Fe(II) sites by Panov et al.: Fe capable of forming an active oxygen that oxidizes benzene (and methane) at room temperature.[2,51]

Here, we quantify α-Fe(II) by its unique doublet with low QS in Mössbauer spectroscopy, as reported earlier.[11,12] Studies have shown that several species of Fe(II) including α-Fe(II), when hydrated, were indistinguishable at low temperature and undetectable at room temperature,[16,52] and this may have affected the quantification of α-Fe(II) in the previous literature. In this work, low-temperature Mössbauer spectra were measured on samples after dry calcination. The leftover hydrated α-Fe(II) doublet are only optionally added into the quantification of α-Fe(II) because it may either be hydrated α-Fe(II) or other hydrated Fe(II). This is why we give a range for α-Fe(II) concentrations rather than single values.

In numerous studies, α-Fe(II) has been quantified by the deposition of oxygen by N_2O on Fe that was not oxidized by O_2 at ~250 °C.[10,36,53−56] While this may give a good indication of isolated Fe(II), it is not a sufficient method to exclusively quantify α-Fe(II),[57,58] and previously reported concentrations of α-Fe(II) on Fe-ZSM-5 have likely been overestimates.[36,56,59] On the other hand, methanol yields from liquid extraction after room temperature CH_4 reaction underestimate α-Fe(II) concentration because further oxidation of methanol is rarely taken into account. It is not known whether the subsequent oxidations occur with α-O or with oxidized spectators, and methanol recovery may be incomplete.

4.2. Methods of Iron Introduction. We introduced iron to H−CHA using aqueous ion exchange or impregnation of various Fe(III) sources and synthesized Fe−CHA directly by adding different Fe(III) sources to the crystallization batch (one-pot methods). At low loadings of iron, the method of introduction does not appear to be of much importance to the final product, both in terms of crystal properties and iron speciation. All techniques yield mostly α-Fe(II) after He treatment at 900 °C. Only when starting from Fe(III) oxides, iron remained largely in its oxide form. Probably any of the commonly used techniques, including solid state exchange, liquid ion exchange, impregnation, and addition of Fe in the hydrothermal synthesis, can be used successfully to prepare α-Fe(II) zeolites from Fe(III) precursors at low Fe loadings.

At higher Fe loadings differences emerge between the different preparation methods. A first point is that high loadings are difficult to achieve using the postsynthesis iron introduction methods demonstrated here. While iron retention can be increased by using zeolites with more Al pairs, postsynthetic Fe exchange does not occur on all existing Al pairs.[60] Based on our experimental work we can state that also the initial dispersion of Fe and the barrier to intracrystalline diffusion now becomes important in determining the final form of Fe. The former may be manipulated by the distribution of Al(III) in the zeolite, the Fe loading, and the Fe precursor. The latter may be manipulated by the zeolite topology and framework Al(III) content, although their importance is subdued by introducing Fe before the crystals have fully formed. This work shows that one-pot preparations of zeolite with Fe in the framework could very selectively be transformed into a nearly single-site α-Fe(II) material. Low initial dispersion and high barriers for subsequent dispersion result in clusters of Fe oxides (≥two Fe atoms) including bulk oxide phases, while the inverse conditions lead to mononuclear α-Fe(II). High loading Fe zeolites prepared in various ways have

Scheme 1. Formation of α-Fe(II) from Fe(III) in a Zeolite Framework Using High Temperature Treatment in Dry, Inert Gas Flow[a]

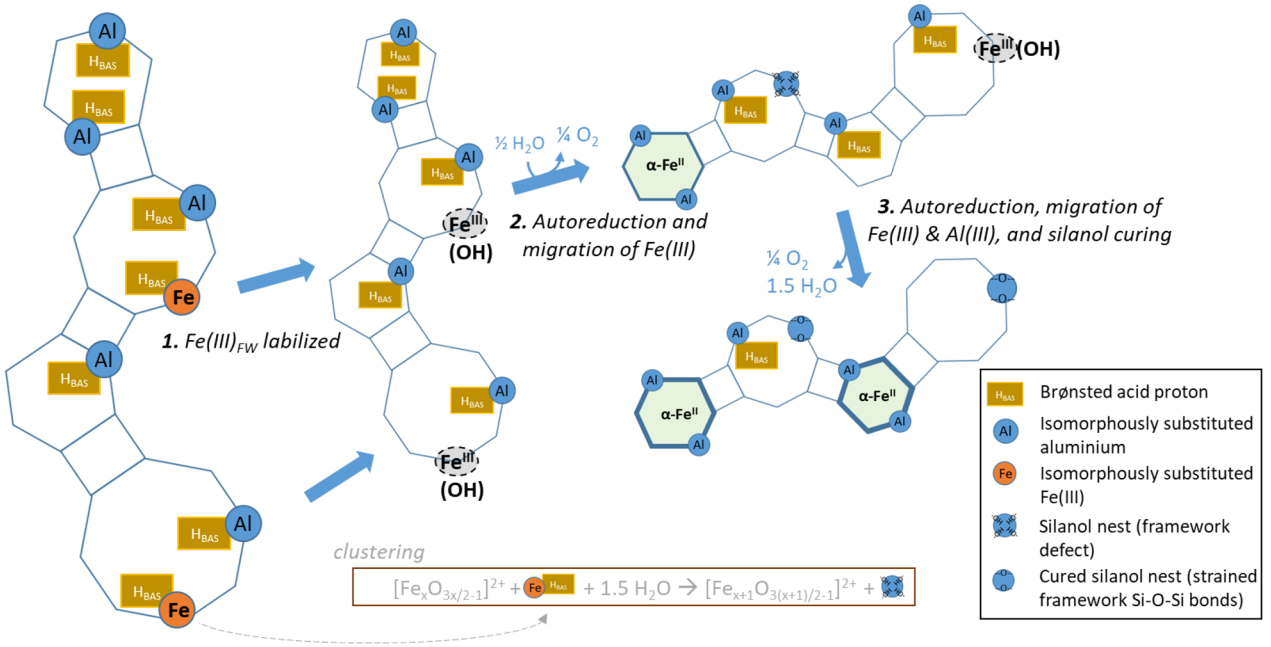

[a]Step 2: formation of first α-Fe(II) cohort. Step 3: formation of second cohort of α-Fe(II).

been investigated, and some have claimed samples that contain mainly Fe(III) dimers that do not autoreduce in vacuum.[16,61] Given their high Fe loadings, the exact characterization of their iron is challenging because likely many forms of iron coexisted. The preparation of single-site Fe-zeolites with well-defined multinuclear Fe oxide clusters remains an open challenge.

4.3. Role of Framework Al(III) Migration. At this stage we have identified the dispersion of Fe, for instance achieved by the one pot method, as a requirement to selectively prepare α-Fe(II). Especially at higher iron loadings, it becomes crucial to turn to techniques that ensure maximal dispersion. To form α-Fe(II), also the substitution of two specific T sites in the 6MR by aluminum is required.[9,11,60] In MFI, these are the T4 and T10 sites, in FER the T1 sites, in *BEA the two T6 or T4 or T8 sites, and in CHA two opposing T1 sites.[11,12,62] The availability of 6MR exchange sites with correct Al_{FW} positioning can rapidly become limiting at elevated iron loadings. On MFI, at Si/Al = 10, a thermodynamically directed Al_{FW} distribution in the absence of divalent cations was predicted to result in 2.1% and 2.3% of total Al_{FW} in the T10 and T4 positions, respectively, or a maximum of only 0.021 α-Fe(II)/Al.[63] Some authors have reported α-site concentrations far above this after steaming or treatment at 900 °C.[36,55,64] Dedecek et al. investigated the Al_{FW} distribution on synthesized CHA ($TMAda^+$ as OSDA, Si/Al = 12). A total of 5% of Al_{FW} was assigned to opposing the T1T1 configuration in a single 6MR,[65] enabling an α-Fe(II) to Al ratio of 0.025. On our baseline one-pot sample ($IZC(^{57}A)_{288}$), Mossbauer indicates at least 72% of Fe forms α-Fe after He 900 °C or an α-Fe(II) to Al ratio greater than 0.15. This far exceeds the boundary based on the Dedecek et al. data. On this sample, 72% α-Fe corresponds to 207 μmol α-Fe(II)/g.

In section 3.4, we describe the formation of α-Fe(II) sites from a mononuclear Fe(III) precursor in two cohorts. The second cohort was formed only at temperature above 850 °C through an irreversible process involving an autoreduction with the release of O_2. We showed the desorption of a quantity of O_2 in the 900 °C treatment comparable to the amount of α-Fe(II) formed (section S6), indicative of the autoreduction of Fe(III). We found that the temperature required for this step was not lowered by forcing reduction in H_2 so that the reduction itself was not the bottleneck (Supporting Information section S4). We also saw that BAS are lost at >850 °C and that O_2 and H_2O are released. These findings combined with observations available from existing literature suggest a mechanism that involves the migration of framework Al(III) to form new α-Fe(II) exchange sites at >850 °C in a dry atmosphere. The additional formation of α-Fe(II) after steaming or treatment at 900 °C coincides with the conditions where aluminum is removed from the framework. This Al forms extra-framework aluminum (Al_{EF}), that may reinsert into the framework.[52,66−69] In MTO conditions (H_2O/methanol at 500 °C), Al_{EF} is incorporated in the MFI framework and migrates through the crystal.[70] On dealuminated *BEA, $Fe(III)_{FW}$ can be built in postsynthetically.[71]

We propose the first cohort of α-Fe(II) is formed in d6rs sites in which suitable Al(III) substitutions to host α-Fe(II) preexisted. This cohort may thus be obtained by synthetic steering toward high Al pairs density (e.g., using IZC[72]). The second cohort, on the other hand, is formed only under conditions that allow a redistribution of framework Al(III). Under such conditions Al(III) and Fe(III) migrate to maximize the formation of thermodynamically preferred α-Fe(II). Direct spectroscopic proof of this migration is difficult to obtain. In contrast to SAPO materials (Si-islanding[73,74]) or gallosilicates,[75] T-atom reshuffling cannot readily be traced by NMR techniques in zeolites and ferrosilicates.[14,76] The further development of novel NMR solutions (potentially challenging with paramagnetic Fe) or a combination of indirect validation methods (e.g., cobalt titration[72]) would be needed.

After dry air calcination below 650 °C and preceding any He 900 °C or steaming treatment, 12 ± 5% of Fe formed α-Fe(II)

(Figure S16), corresponding to 0.028 ± 0.012 α-Fe(II) per Al. This is in good agreement with the concentration of 6MR with opposing Al_{FW} measured by Dedecek et al. after synthesis and calcination. It is therefore reasonable that the first α-Fe(II) cohort occupies only the originally available opposing T1T1 Al substitutions. After treatment at 900 °C, the >0.18 α-Fe(II)/Al requires more than 36% of available Al to be specifically positioned in opposing T1 sites of a single 6MR. This even surpasses the Al pairing (of any configuration) that can be expected statistically (16% at Si/Al = 15)[77] after synthesis and calcination in rigid frameworks and again supports the hypothesis of Al_{FW} relocation at high temperature or steaming to enable thermodynamically favorable α-Fe(II) speciation.[78]

Note that the mechanism of Al_{FW} relocation is not fully understood. Likely, defects relocate due to expulsion/reinsertion of both Si and Al_{FW} hydrolyzed species from/into the framework.[79,80] It is not fully clear whether defects must be already present. If so, the irreversible curing of silanol nests at elevated temperatures, immediately removing the open T-site upon expulsion of Al_{FW}, may interfere with Al relocation, preventing complete transformation to α-Fe(II) at high loadings. Note that forming new silanol nests requires external H_2O supply, which should no longer be available in helium at 900 °C.

4.4. Model for α-Fe(II) Formation. The processes leading to α-Fe(II) are integrated in Scheme 1. We start from a zeolite with Fe(III) in framework positions and with the cation exchange capacity generated by Fe(III) and Al(III) substitution fully compensated by BAS. In reality, ion exchange capacity is initially compensated by cations used in synthesis and template molecules that are burned off to leave BAS, but we omit this for clarity. We also leave out the desorption of H_2O for the same reason. These two processes occur simultaneously with the labilization of framework Fe(III), enabling its relocation to extra-framework exchange sites (step 1). Its transformation to Fe species in ion exchange positions in the presence of aluminum in the framework was also considered, but we did not find suitable DFT models for such structures that are in agreement with the spectroscopic data.[18,43,52,81] In MFI silicalite, framework Fe(III) is nearly fully converted to Fe_2O_3 at 700 °C.[43] The removal of Al_{FW} or $Fe(III)_{FW}$ introduces silanol nests, but the three-dimensional structure of zeolites can be maintained even after high degrees of T-atom removal.[76] From our experiments and DFT models, we propose that the extracted Fe(III) likely forms partially extruded framework Fe(III) with an unaltered elemental composition. Alternatively, $Fe(III)_{FW}$ can form clusters in the presence of H_2O through the reaction shown by the box at the bottom of Scheme 1.

In step 2, a first fraction of Fe(III) is transformed into the first cohort of α-Fe(II) provided it can diffuse to suitable preexisting ion exchange sites with a double Al(III) substitution. This encompasses the one electron autoreduction of Fe(III) to Fe(II) and releases 1/4 O_2 per formed α-Fe(II). It has been repeatedly observed that the autoreduction of Fe(III) to α-Fe(II) cannot be reversed with O_2.[11,12,56] Also on the CHA materials in this study, we observe the stability of α-Fe(II) under an O_2 atmosphere (Supporting Information section S4). Other authors have proposed a model where Fe in dimeric clusters is spatially separated, and the separated Fe sites can no longer react with O_2; however, our Mössbauer data indicate an isolated mononuclear Fe(III) precursor.[56] In step 3, the second α-Fe(II) cohort is generated at 900 °C, as discussed in full in section 4.3. Its formation depends on the migration of Al to form T1T1 substituted pairs in 6MRs. As suitable T1T1 exchange sites become available, Fe(III) species are fully extruded from the lattice and autoreduced to form isolated α-Fe(II). Simultaneously, silanol nests are (partially) cured to bridged siloxanes, releasing H_2O. Here we assume that Si migrates parallel to Al and takes the original place of the migrated Al in the framework. This is the simplest explanation but remains to be verified. Based on current data, we cannot distinguish α-Fe(II) formed in the first cohort from α-Fe(II) formed in the second cohort once they are formed. Likely a similar scheme is followed for different zeolite topologies (see section S9).

5. CONCLUSION

We achieved the introduction of α-Fe(II) loadings up to and above a record 207 μmol/g on CHA zeolite. This corresponds to >72% of all iron in the sample as Fe(II). Essential to achieve this is the one-pot synthesis strategy, where iron, as an Fe salt, is introduced in the zeolite synthesis mixture prior to crystallization. The one-pot strategy was needed to enable high loadings of well-dispersed mononuclear iron cations into the zeolite. High dispersion allows easy access to exchange sites preventing the aggregation of iron into oxide clusters. To form α-Fe(II) sites, a specific T1T1 configuration of paired Al substitutions in a 6MR is required. Such T1T1 configurations are formed already in limited amounts in the synthesized zeolite, and we find accordingly that a limited concentration of α-Fe(II) sites is formed after dry calcination. The α-Fe(II) sites should therefore also be considered as optional active sites in Fe zeolite catalysis where no further activation steps have been applied, especially when Fe loadings are low. In high Fe loaded zeolites, the limited concentration of T1T1 Al pairs is a bottleneck to the formation of additional α-Fe(II) sites. By activating the material at temperatures >850 °C, the exchange site bottleneck is mediated by mobilization of Al, driven by thermodynamic benefits of the α-Fe(II)/2Al ensemble. Water is required in the initial removal of Fe(III) from the framework, and the full liberation of Fe(III) from the framework depends on the presence of T1T1 configurations of paired Al substitutions. Moreover water is a reagent in the direct formation of oxide clusters from framework iron. To minimize clustering, excess water is therefore best avoided, especially on materials with high Fe loadings, low Fe dispersion, or high Si/Al.

The ability to introduce α-Fe(II) at high concentration and purity into zeolites holds promise for better catalysts for N_2O and NO_X abatement and (partial) oxidation catalysis. Here, the high α-Fe(II) loadings could be translated to stoichiometric methanol yields up to 183 μmol/g, a large improvement from the previously reported 70 μmol/g record on Fe zeolites.[10] Besides enabling better catalytic performance, the high α-Fe(II) site loading and purity will allow for more sensitive mechanistic catalysis studies. Further improvement to higher loadings and purity of α-Fe(II) is likely obstructed by the failure of one-pot preparations with organic template to crystallize into Fe(Al)−CHA at higher iron concentrations (considering Fe(III) enters the framework) and lower Si/Al ratios in the absence of Na^+.

■ ASSOCIATED CONTENT

Supporting Information

The Supporting Information is available free of charge at .

Details on zeolite synthesis and additional experimental variations, in-depth characterization and discussions of one-pot zeolites, detailed discussion on the stoichiometry going from α-Fe(II) to α-O to extractable methanol, additional gas phase tests on iron species, comparison between the outcome of IZC and synthesis from amorphous Al and Si sources, mass spectrometry data on the gas phase treatment steps, analysis of the spectra in the NIR region, FT-IR spectroscopy, deconvolution of Mössbauer spectra, comparison between large pore *BEA and small pore CHA, effect of Na^+ in the one pot synthesis on the formation of α-Fe(II), DFT calculations, and model Mössbauer parameters (PDF)

■ AUTHOR INFORMATION

Corresponding Authors

Michiel Dusselier − *Department of Microbial and Molecular Systems, KU Leuven, 3001 Heverlee, Belgium;* orcid.org/0000-0002-3074-2318; Email: michiel.dusselier@kuleuven.be

Robert A. Schoonheydt − *Department of Microbial and Molecular Systems, KU Leuven, 3001 Heverlee, Belgium*; Email: robert.schoonheydt@kuleuven.be

Edward I. Solomon − *Department of Chemistry, Stanford University, Stanford, California 94305, United States;* orcid.org/0000-0003-0291-3199; Email: edward.solomon@stanford.edu

Bert F. Sels − *Department of Microbial and Molecular Systems, KU Leuven, 3001 Heverlee, Belgium;* orcid.org/0000-0001-9657-1710; Email: bert.sels@kuleuven.be

Authors

Max L. Bols − *Department of Microbial and Molecular Systems, KU Leuven, 3001 Heverlee, Belgium;* orcid.org/0000-0002-4576-5969

Julien Devos − *Department of Microbial and Molecular Systems, KU Leuven, 3001 Heverlee, Belgium;* orcid.org/0000-0002-2254-9016

Hannah M. Rhoda − *Department of Chemistry, Stanford University, Stanford, California 94305, United States;* orcid.org/0000-0001-5730-5209

Dieter Plessers − *Department of Microbial and Molecular Systems, KU Leuven, 3001 Heverlee, Belgium*

Complete contact information is available at:

Author Contributions

§ M.L.B. and J.D. contributed equally to this work.

Funding

Funding for this work was provided by the Flemish Research Foundation (FWO, Grant G0A2216N to B.F.S. and R.A.S., Travel Grant V417018N to M.L.B., and Postdoctoral Fellowship 1276021N to M.L.B.) and the National Science Foundation (NSF, Grant CHE-1660611 to E.I.S.). M.D. acknowledges KU Leuven BOFZAP for his appointment.

Notes

The authors declare no competing financial interest.

■ ACKNOWLEDGMENTS

We thank Dr. Sonjong Hwang from the California Institute of Technology (Cal, U.S.) for recording the NMR spectra, SACHEM for providing the organic structure-directing agents (TMAdaOH), and Janne Gys for preparing the one-pot Na−CHA.

■ ABBREVIATIONS

acac, acetylacetonate; Al_{EF}, extraframework aluminum; Al_{FW}, framework aluminum; BAS, Brönsted acid site(s); *BEA, beta zeolite; CHA, chabazite zeolite; CT, charge transfer; DR, diffuse reflectance; EPT, electron pair transition; FAU, faujazite zeolite; $Fe(III)_{FW}$, framework iron; FER, ferrierite zeolite; FT-IR, Fourier transform infrared spectroscopy; IS, isomer shift; IZC, interzeolite conversion; KM, Kubelka−Munk transformed; MFI, ZSM-5 framework type; MR, membered ring; MS, mass spectrometry; MTO, methanol to olefins; O_{EF}^{2-}, oxygen ligands not part of the zeolite framework; OSDA, organic structure directing agent; P-XRD, powder X-ray diffraction; QS, quadrupole splitting; SCR, selective catalytic reduction; T#, specific crystallographic framework position in a zeolite; $TMAda^+$, trimethyladamantylammonium; UV−vis-NIR, UV−visible-near-infrared absorption spectroscopy; ZSM-5, zeolite Socony Mobil-5

■ REFERENCES

(1) Pannov, G.I.; Sobolev, V.I.; Kharitonov, A.S. The Role of Iron in N2O Decomposition on ZSM-5 Zeolite and Reactivity of the Surface Oxygen Formed. *J. Mol. Catal.* **1990**, *61*, 85−97.

(2) Panov, G. I.; Sheveleva, G. A.; Kharitonov, A. S.; Romannikov, V. N.; Vostrikova, L. A. Oxidation of Benzene to Phenol by Nitrous Oxide over Fe-ZSM-5 Zeolites. *Appl. Catal., A* **1992**, *82*, 31−36.

(3) Sobolev, V. I.; Panov, G. I.; Kharitonov, A. S.; Romannikov, V. N.; Volodin, A. M.; Ione, K. G. Catalytic Properties of ZSM-5 Zeolites in N2O Decomposition: The Role of Iron. *J. Catal.* **1993**, *139*, 435−443.

(4) Høj, M.; Beier, M. J.; Grunwaldt, J. D.; Dahl, S. The Role of Monomeric Iron during the Selective Catalytic Reduction of NOx by NH3 over Fe-BEA Zeolite Catalysts. *Appl. Catal., B* **2009**, *93*, 166−176.

(5) Zhu, Y.; Chen, B.; Zhao, R.; Zhao, Q.; Gies, H.; Xiao, F. S.; De Vos, D.; Yokoi, T.; Bao, X.; Kolb, U.; Feyen, M.; Maurer, S.; Moini, A.; Müller, U.; Shi, C.; Zhang, W. Fe-Doped Beta Zeolite from Organotemplate-Free Synthesis for NH3-SCR of NOx. *Catal. Sci. Technol.* **2016**, *6*, 6581−6592.

(6) Shi, J.; Zhang, Y.; Zhu, Y.; Chen, M.; Zhang, Z.; Shangguan, W. Efficient Fe-ZSM-5 Catalyst with Wide Active Temperature Window for NH3 Selective Catalytic Reduction of NO: Synergistic Effect of Isolated Fe3+ and Fe2O3. *J. Catal.* **2019**, *378*, 17−27.

(7) Bols, M. L.; Rhoda, H. M.; Snyder, B. E. R.; Solomon, E. I.; Pierloot, K.; Schoonheydt, R. A.; Sels, B. F. Advances in the Synthesis, Characterisation, and Mechanistic Understanding of Active Sites in Fe-Zeolites for Redox Catalysts. *Dalt. Trans.* **2020**, *49*, 14749−14757.

(8) Bols, M. L.; Snyder, B. E. R.; Rhoda, H. M.; Cnudde, P.; Fayad, G.; Schoonheydt, R. A.; Van Speybroeck, V.; Solomon, E. I.; Sels, B. F. Coordination and Activation of Nitrous Oxide by Iron Zeolites. *Nat. Catal.* **2021**, *4*, 332−340.

(9) Snyder, B. E. R.; Böttger, L. H.; Bols, M. L.; Yan, J. J.; Rhoda, H. M.; Jacobs, A. B.; Hu, M. Y.; Zhao, J.; Alp, E. E.; Hedman, B.; Hodgson, K. O.; Schoonheydt, R. A.; Sels, B. F.; Solomon, E. I. Structural Characterization of a Non-Heme Iron Active Site in Zeolites That Hydroxylates Methane. *Proc. Natl. Acad. Sci. U. S. A.* **2018**, *115*, 4565−4570.

(10) Starokon, E. V.; Parfenov, M. V.; Pirutko, L. V.; Abornev, S. I.; Panov, G. I. Room-Temperature Oxidation of Methane by α-Oxygen

and Extraction of Products from the FeZSM-5 Surface. *J. Phys. Chem. C* **2011**, *115*, 2155−2161.
(11) Bols, M. L.; Hallaert, S. D.; Snyder, B. E. R.; Devos, J.; Plessers, D.; Rhoda, H. M.; Dusselier, M.; Schoonheydt, R. A.; Pierloot, K.; Solomon, E. I.; Sels, B. F. Spectroscopic Identification of the α-Fe/α-O Active Site in Fe-CHA Zeolite for the Low-Temperature Activation of the Methane C-H Bond. *J. Am. Chem. Soc.* **2018**, *140*, 12021−12032.
(12) Snyder, B. E. R.; Vanelderen, P.; Bols, M. L.; Hallaert, S. D.; Böttger, L. H.; Ungur, L.; Pierloot, K.; Schoonheydt, R. A.; Sels, B. F.; Solomon, E. I. The Active Site of Low-Temperature Methane Hydroxylation in Iron-Containing Zeolites. *Nature* **2016**, *536*, 317−321.
(13) Dusselier, M.; Davis, M. E. Small-Pore Zeolites: Synthesis and Catalysis. *Chem. Rev.* **2018**, *118*, 5265−5329.
(14) Schmidt, J. E.; Oord, R.; Guo, W.; Poplawsky, J. D.; Weckhuysen, B. M. Nanoscale Tomography Reveals the Deactivation of Automotive Copper-Exchanged Zeolite Catalysts. *Nat. Commun.* **2017**, *8*, 1666.
(15) Gao, F.; Zheng, Y.; Kukkadapu, R. K.; Wang, Y.; Walter, E. D.; Schwenzer, B.; Szanyi, J.; Peden, C. H. F. Iron Loading Effects in Fe/SSZ-13 NH3-SCR Catalysts: Nature of the Fe Ions and Structure-Function Relationships. *ACS Catal.* **2016**, *6*, 2939−2954.
(16) Gao, F.; Kollár, M.; Kukkadapu, R. K.; Washton, N. M.; Wang, Y.; Szanyi, J.; Peden, C. H. F. Fe/SSZ-13 as an NH3-SCR Catalyst: A Reaction Kinetics and FTIR/Mössbauer Spectroscopic Study. *Appl. Catal., B* **2015**, *164*, 407−419.
(17) Snyder, B. E. R.; Bols, M. L.; Rhoda, H. M.; Plessers, D.; Schoonheydt, R. A.; Sels, B. F.; Solomon, E. I. Cage Effects Control the Mechanism of Methane Hydroxylation in Zeolites. *Science (Washington, DC, U. S.)* **2021**, *373*, 327−331.
(18) Martín, N.; Vennestrøm, P. N. R.; Thøgersen, J. R.; Moliner, M.; Corma, A. Fe-Containing Zeolites for NH3-SCR of NOx: Effect of Structure, Synthesis Procedure, and Chemical Composition on Catalytic Performance and Stability. *Chem. - Eur. J.* **2017**, *23*, 13404−1341.
(19) Perez-Ramirez, J.; Groen, J.; Bruckner, A.; Kumar, M.; Bentrup, U.; Debbagh, M.; Villaescusa, L. Evolution of Isomorphously Substituted Iron Zeolites during Activation: Comparison of Fe-Beta and Fe-ZSM-5. *J. Catal.* **2005**, *232*, 318−334.
(20) Mahyuddin, M. H.; Shiota, Y.; Yoshizawa, K. Methane Selective Oxidation to Methanol by Metal-Exchanged Zeolites: A Review of Active Sites and Their Reactivity. *Catal. Sci. Technol.* **2019**, *9*, 1744−1768.
(21) Knorpp, A. J.; Pinar, A. B.; Newton, M. A.; Sushkevich, V. L.; van Bokhoven, J. A. Copper-Exchanged Omega (MAZ) Zeolite: Copper-Concentration Dependent Active Sites and Its Unprecedented Methane to Methanol Conversion. *ChemCatChem* **2018**, *10*, 5593−5596.
(22) Frisch, M. J.; Trucks, G. W.; Schlegel, H. B.; Scuseria, G. E.; Robb, M. A.; Cheeseman, J. R.; Scalmani, G.; Barone, V.; Petersson, G. A.; Nakatsuji, H.; Li, X.; Caricato, M.; Marenich, A. V.; Bloino, J.; Janesko, B. G.; Gomperts, R.; Mennucci, B.; Hratchian, H. P.; Ortiz, J. V.; Izmaylov, A. F.; Sonnenberg, J. L.; Williams-Young, D.; Ding, F.; Lipparini, F.; Egidi, F.; Goings, J.; Peng, B.; Petrone, A.; Henderson, T.; Ranasinghe, D.; Zakrzewski, V. G.; Gao, J.; Rega, N.; Zheng, G.; Liang, W.; Hada, M.; Ehara, M.; Toyota, K.; Fukuda, R.; Hasegawa, J.; Ishida, M.; Nakajima, T.; Honda, Y.; Kitao, O.; Nakai, H.; Vreven, T.; Throssell, K.; Montgomery, J. A., Jr.; Peralta, J. E.; Ogliaro, F.; Bearpark, M. J.; Heyd, J. J.; Brothers, E. N.; Kudin, K. N.; Staroverov, V. N.; Keith, T. A.; Kobayashi, R.; Normand, J.; Raghavachari, K.; Rendell, A. P.; Burant, J. C.; Iyengar, S. S.; Tomasi, J.; Cossi, M.; Millam, J. M.; Klene, M.; Adamo, C.; Cammi, R.; Ochterski, J. W.; Martin, R. L.; Morokuma, K.; Farkas, O.; Foresman, J. B.; Fox, D. J. *Gaussian 16*, Revision C.01; Gaussian, Inc.: Wallingford, CT, 2016.
(23) Grimme, S.; Antony, J.; Ehrlich, S.; Krieg, H. A Consistent and Accurate Ab Initio Parametrization of Density Functional Dispersion Correction (DFT-D) for the 94 Elements H-Pu. *J. Chem. Phys.* **2010**, *132*, 154104.
(24) Neese, F. The ORCA Program System. Wiley Interdiscip. *Wiley Interdiscip. Rev.: Comput. Mol. Sci.* **2012**, *2*, 73−78.
(25) Neese, F. Prediction and Interpretation of the 57Fe Isomer Shift in Mössbauer Spectra by Density Functional Theory. *Inorg. Chim. Acta* **2002**, *337*, 181−192.
(26) Martín, N.; Vennestrøm, P. N. R.; Thøgersen, J. R.; Moliner, M.; Corma, A. Iron-Containing SSZ-39 (AEI) Zeolite: An Active and Stable High-Temperature NH3-SCR Catalyst. *ChemCatChem* **2017**, *9*, 1754−1757.
(27) Yin, C.; Cheng, P.; Li, X.; Yang, R. T. Selective Catalytic Reduction of Nitric Oxide with Ammonia over High-Activity Fe/SSZ-13 and Fe/One-Pot-Synthesized Cu-SSZ-13 Catalysts. *Catal. Sci. Technol.* **2016**, *6*, 7561−7568.
(28) Xie, L.; Liu, F.; Ren, L.; Shi, X.; Xiao, F. S.; He, H. Excellent Performance of One-Pot Synthesized Cu-SSZ-13 Catalyst for the Selective Catalytic Reduction of NOx with NH3. *Environ. Sci. Technol.* **2014**, *48*, 566−572.
(29) Niu, K.; Li, G.; Liu, J.; Wei, Y. One Step Synthesis of Fe-SSZ-13 Zeolite by Hydrothermal Method. *J. Solid State Chem.* **2020**, *287*, 121330.
(30) Fickel, D. W.; Lobo, R. F. Copper Coordination in Cu-SSZ-13 and Cu-SSZ-16 Investigated by Variable-Temperature XRD. *J. Phys. Chem. C* **2010**, *114*, 1633−1640.
(31) Li, S.; Li, H.; Gounder, R.; Debellis, A.; Müller, I. B.; Prasad, S.; Moini, A.; Schneider, W. F. First-Principles Comparison of Proton and Divalent Copper Cation Exchange Energy Landscapes in SSZ-13 Zeolite. *J. Phys. Chem. C* **2018**, *122*, 23564−23573.
(32) Chen, H.-Y.; Sachtler, W. M. Activity and Durability of Fe/ZSM-5 Catalysts for Lean Burn NOx Reduction in the Presence of Water Vapor. *Catal. Today* **1998**, *42*, 73−83.
(33) Voskoboinikov, T. V.; Chen, H. Y.; Sachtler, W. M. H. On the Nature of Active Sites in Fe/ZSM-5 Catalysts for NO(χ) Abatement. *Appl. Catal., B* **1998**, *19*, 279−287.
(34) Feng, X.; Keith Hall, W. FeZSM-5: A Durable SCR Catalyst for NOxRemoval from Combustion Streams. *J. Catal.* **1997**, *166*, 368−376.
(35) Gallup, D. L. Aluminum Silicate Scale Formation and Inhibitor (2): Scale Solubilities and Laboratory and Field Inhibition Tests. *Geothermics* **1998**, *27*, 485−501.
(36) Dubkov, K. A.; Ovanesyan, N. S.; Shteinman, A. A.; Starokon, E. V.; Panov, G. I. Evolution of Iron States and Formation of α-Sites upon Activation of FeZSM-5 Zeolites. *J. Catal.* **2002**, *207*, 341−352.
(37) Lázár, K.; Pozdnyakova, O.; Wootsch, A.; Fejes, P. Iron Ions in ZSM-5 Zeolite: Fe3+ in Framework, Fe2+ in Extra-Framework Positions in Catalytic N2O Decomposition. *Hyperfine Interact.* **2006**, *167*, 779−784.
(38) Lázár, K.; Vincent, C.; Fejes, P. Variety of Available Coordination Sites for Extra-Framework Iron in LTA and MFI Zeolites. *Hyperfine Interact.* **2008**, *187*, 1−6.
(39) Mørup, S.; Knudsen, J. E.; Nielsen, M. K.; Trumpy, G. Mössbauer Spectroscopic Studies of Frozen Aqueous Solutions of Fe 3+ Salts. *J. Chem. Phys.* **1976**, *65*, 536−543.
(40) Goldfarb, D.; Bernardo, M.; Strohmaier, K. G.; Vaughan, D. E. W.; Thomann, H. Characterization of Iron in Zeolites by X-Band and Q-Band ESR, Pulsed ESR, and UV-Visible Spectroscopies. *J. Am. Chem. Soc.* **1994**, *116*, 6344−6353.
(41) Patarin, J.; Tuilier; Durr, J.; Kessler, H. Optical and X-Ray Absorption Spectroscopy Studies of Iron MFI-Type Zeolite Prepared in Fluoride Medium. *Zeolites* **1992**, *12*, 70−75.
(42) Sun, K.; Fan, F.; Xia, H.; Feng, Z.; Li, W. X.; Li, C. Framework Fe Ions in Fe-ZSM-5 Zeolite Studied by UV Resonance Raman Spectroscopy and Density Functional Theory Calculations. *J. Phys. Chem. C* **2008**, *112*, 16036−16041.
(43) Bordiga, S.; Buzzoni, R.; Geobaldo, F.; Lamberti, C.; Giamello, E.; Zecchina, A.; Leofanti, G.; Petrini, G.; Tozzola, G.; Vlaic, G. Structure and Reactivity of Framework and Extraframework Iron in Fe-Silicalite as Investigated by Spectroscopic and Physicochemical Methods. *J. Catal.* **1996**, *158*, 486−501.

(44) Pirngruber, G. D.; Roy, P. K.; Prins, R. On Determining the Nuclearity of Iron Sites in Fe-ZSM-5 - A Critical Evaluation. *Phys. Chem. Chem. Phys.* **2006**, *8*, 3939−3950.
(45) Nielsen, M.; Brogaard, R. Y.; Falsig, H.; Beato, P.; Swang, O.; Svelle, S. Kinetics of Zeolite Dealumination: Insights from H-SSZ-13. *ACS Catal.* **2015**, *5*, 7131−7139.
(46) Silaghi, M.-C.; Chizallet, C.; Sauer, J.; Raybaud, P. Dealumination Mechanisms of Zeolites and Extra-Framework Aluminum Confinement. *J. Catal.* **2016**, *339*, 242−255.
(47) Stanciakova, K.; Ensing, B.; Göltl, F.; Bulo, R. E.; Weckhuysen, B. M. Cooperative Role of Water Molecules during the Initial Stage of Water-Induced Zeolite Dealumination. *ACS Catal.* **2019**, *9*, 5119−5135.
(48) Sherman, D. M.; Waite, T. D.; Waite, D. T. Electronic Spectra of Fe3+ + Oxides and Oxide Hydroxides in the near IR to near UV. *Am. Mineral.* **1985**, *70*, 1262−1269.
(49) Marusak, L. A.; Messier, R.; White, W. B. Optical Absorption Spectrum of Hematite, AFe2O3 near IR to UV. *J. Phys. Chem. Solids* **1980**, *41*, 981−984.
(50) Dubkov, K. A.; Paukshtis, E. A.; Panov, G. I. Stoichiometry of Oxidation Reactions Involving α-Oxygen on FeZSM-5 Zeolite. *Kinet. Catal.* **2001**, *42*, 205−211.
(51) Dubkov, K. A.; Sobolev, V. I.; Panov, G. I. Low-Temperature Oxidation of Methane to Methanol on FeZSM-5 Zeolite. *Kinet. Catal.* **1998**, *39*, 72−79.
(52) Taboada, J. B.; Overweg, A. R.; Kooyman, P. J.; Arends, I. W. C. E.; Mul, G. Following the Evolution of Iron from Framework to Extra-Framework Positions in Isomorphously Substituted [Fe,Al]MFI with 57Fe Mössbauer Spectroscopy. *J. Catal.* **2005**, *231*, 56−66.
(53) Wood, B. R.; Reimer, J. A.; Bell, A. T.; Janicke, M. T.; Ott, K. C. Nitrous Oxide Decomposition and Surface Oxygen Formation on Fe-ZSM-5. *J. Catal.* **2004**, *224*, 148−155.
(54) Starokon, E. V.; Parfenov, M. V.; Arzumanov, S. S.; Pirutko, L. V.; Stepanov, A. G.; Panov, G. I. Oxidation of Methane to Methanol on the Surface of FeZSM-5 Zeolite. *J. Catal.* **2013**, *300*, 47−54.
(55) Parfenov, M. V.; Starokon, E. V.; Pirutko, L. V.; Panov, G. I. Quasicatalytic and Catalytic Oxidation of Methane to Methanol by Nitrous Oxide over FeZSM-5 Zeolite. *J. Catal.* **2014**, *318*, 14−21.
(56) Starokon, E. V.; Dubkov, K. A.; Pirutko, L. V.; Panov, G. I. Mechanisms of Iron Activation on Fe-Containing Zeolites and the Charge of α-Oxygen. *Top. Catal.* **2003**, *23*, 137−143.
(57) Kiwi-Minsker, L.; Bulushev, D. A.; Renken, A. Active Sites in HZSM-5 with Low Fe Content for the Formation of Surface Oxygen by Decomposing N2O: Is Every Deposited Oxygen Active? *J. Catal.* **2003**, *219*, 273−285.
(58) Kondratenko, E. V.; Pérez-Ramírez, J. Mechanism and Kinetics of Direct N2O Decomposition over Fe-MFI Zeolites with Different Iron Speciation from Temporal Analysis of Products. *J. Phys. Chem. B* **2006**, *110*, 22586−22595.
(59) Ivanov, D. P.; Pirutko, L. V.; Panov, G. I. Effect of Steaming on the Catalytic Performance of ZSM-5 Zeolite in the Selective Oxidation of Phenol by Nitrous Oxide. *J. Catal.* **2014**, *311*, 424−432.
(60) Devos, J.; Bols, M. L.; Plessers, D.; Van Goethem, C.; Seo, J. W.; Hwang, S.-J.; Sels, B. F.; Dusselier, M. Synthesis−Structure−Activity Relations in Fe-CHA for C−H Activation: Control of Al Distribution by Interzeolite Conversion. *Chem. Mater.* **2020**, *32*, 273−285.
(61) Hammond, C.; Forde, M. M.; Ab Rahim, M. H.; Thetford, A.; He, Q.; Jenkins, R. L.; Dimitratos, N.; Lopez-Sanchez, J. A.; Dummer, N. F.; Murphy, D. M.; Carley, A. F.; Taylor, S. H.; Willock, D. J.; Stangland, E. E.; Kang, J.; Hagen, H.; Kiely, C. J.; Hutchings, G. J. Direct Catalytic Conversion of Methane to Methanol in an Aqueous Medium by Using Copper-Promoted Fe-ZSM-5. *Angew. Chem., Int. Ed.* **2012**, *51*, 5129−5133.
(62) Hallaert, S. D.; Bols, M. L.; Vanelderen, P.; Schoonheydt, R. A.; Sels, B. F.; Pierloot, K. Identification of α-Fe in High-Silica Zeolites on the Basis of Ab Initio Electronic Structure Calculations. *Inorg. Chem.* **2017**, *56*, 10681−10690.
(63) Rice, M. J.; Chakraborty, A. K.; Bell, A. T. Site Availability and Competitive Siting of Divalent Metal Cations in ZSM-5. *J. Catal.* **2000**, *194*, 278−285.
(64) Starokon, E. V.; Parfenov, M. V.; Malykhin, S. E.; Panov, G. I. Catalytic Role of O •- Radicals in the Low-Temperature Isotopic Exchange in Dioxygen. *J. Phys. Chem. C* **2011**, *115*, 12554−12559.
(65) Mlekodaj, K.; Dedecek, J.; Pashkova, V.; Tabor, E.; Klein, P.; Urbanova, M.; Karcz, R.; Sazama, P.; Whittleton, S. R.; Thomas, H. M.; Fishchuk, A. V.; Sklenak, S. Al Organization in the SSZ-13 Zeolite. Al Distribution and Extraframework Sites of Divalent Cations. *J. Phys. Chem. C* **2019**, *123*, 7968−7987.
(66) Sun, K.; Zhang, H.; Xia, H.; Lian, Y.; Li, Y.; Feng, Z.; Ying, P.; Li, C. Enhancement of Alpha-Oxygen Formation and N2O Decomposition on Fe/ZSM-5 Catalysts by Extraframework Al. *Chem. Commun. (Cambridge, U. K.)* **2004**, *21*, 2480−2481.
(67) Pérez-Ramírez, J.; Mul, G.; Kapteijn, F.; Moulijn, J. A.; Overweg, A. R.; Doménech, A.; Ribera, A.; Arends, I. W. C. E. Physicochemical Characterization of Isomorphously Substituted FeZSM-5 during Activation. *J. Catal.* **2002**, *207*, 113−126.
(68) Hensen, E. J. M.; Zhu, Q.; Van Santen, R. A. Extraframework Fe-Al-O Species Occluded in MFI Zeolite as the Active Species in the Oxidation of Benzene to Phenol with Nitrous Oxide. *J. Catal.* **2003**, *220*, 260−264.
(69) Sun, K.; Xia, H.; Hensen, E.; Van Santen, R.; Li, C. Chemistry of N2O Decomposition on Active Sites with Different Nature: Effect of High-Temperature Treatment of Fe/ZSM-5. *J. Catal.* **2006**, *238*, 186−195.
(70) Li, J.; Liu, M.; Guo, X.; Dai, C.; Xu, S.; Wei, Y.; Liu, Z.; Song, C. In Situ Aluminum Migration into Zeolite Framework during Methanol-To-Propylene Reaction: An Innovation to Design Superior Catalysts. *Ind. Eng. Chem. Res.* **2018**, *57*, 8190−8199.
(71) Gurgul, J.; Łatka, K.; Hnat, I.; Rynkowski, J.; Dzwigaj, S. Identification of Iron Species in FeSiBEA by DR UV−Vis, XPS and Mössbauer Spectroscopy: Influence of Fe Content. *Microporous Mesoporous Mater.* **2013**, *168*, 1−6.
(72) Devos, J.; Robijns, S.; Van Goethem, C.; Khalil, I.; Dusselier, M. Interzeolite Conversion and the Role of Aluminum: Toward Generic Principles of Acid Site Genesis and Distributions in ZSM-5 and SSZ-13. *Chem. Mater.* **2021**, *33*, 2516−2531.
(73) Minova, I. B.; Barrow, N. S.; Sauerwein, A. C.; Naden, A. B.; Cordes, D. B.; Slawin, A. M. Z.; Schuyten, S. J.; Wright, P. A. Silicon Redistribution, Acid Site Loss and the Formation of a Core−Shell Texture upon Steaming SAPO-34 and Their Impact on Catalytic Performance in the Methanol-to-Olefins (MTO) Reaction. *J. Catal.* **2021**, *395*, 425−444.
(74) Gómez-Hortigüela, L.; Márquez-Álvarez, C.; Grande-Casas, M.; García, R.; Pérez-Pariente, J. Tailoring the Acid Strength of Microporous Silicoaluminophosphates through the Use of Mixtures of Templates: Control of the Silicon Incorporation Mechanism. *Microporous Mesoporous Mater.* **2009**, *121*, 129−137.
(75) Shin, J.; Ahn, N. H.; Camblor, M. A.; Cho, S. J.; Hong, S. B. Intraframework Migration of Tetrahedral Atoms in a Zeolite. *Angew. Chem., Int. Ed.* **2014**, *53*, 8949−8952.
(76) Kovarik, L.; Washton, N. M.; Kukkadapu, R.; Devaraj, A.; Wang, A.; Wang, Y.; Szanyi, J.; Peden, C. H. F.; Gao, F. Transformation of Active Sites in Fe/SSZ-13 SCR Catalysts during Hydrothermal Aging: A Spectroscopic, Microscopic, and Kinetics Study. *ACS Catal.* **2017**, *7*, 2458−2470.
(77) Verma, A. A.; Bates, S. A.; Anggara, T.; Paolucci, C.; Parekh, A. A.; Kamasamudram, K.; Yezerets, A.; Miller, J. T.; Delgass, W. N.; Schneider, W. F.; Ribeiro, F. H. NO Oxidation: A Probe Reaction on Cu-SSZ-13. *J. Catal.* **2014**, *312*, 179−190.
(78) Chow, Y. K.; Dummer, N. F.; Carter, J. H.; Williams, C.; Shaw, G.; Willock, D. J.; Taylor, S. H.; Yacob, S.; Meyer, R. J.; Bhasin, M. M.; Hutchings, G. J. Investigating the Influence of Acid Sites in Continuous Methane Oxidation with N2O over Fe/MFI Zeolites. *Catal. Sci. Technol.* **2018**, *8*, 154−163.

(79) Ikeda, T.; Inagaki, S.; Hanaoka, T. A.; Kubota, Y. Investigation of Si Atom Migration in the Framework of MSE-Type Zeolite YNU-2. *J. Phys. Chem. C* **2010**, *114*, 19641−19648.
(80) Ong, L. H.; Dömök, M.; Olindo, R.; Van Veen, A. C.; Lercher, J. A. Dealumination of HZSM-5 via Steam-Treatment. *Microporous Mesoporous Mater.* **2012**, *164*, 9−20.
(81) Pirutko, L. V.; Chernyavsky, V. S.; Uriarte, A. K.; Panov, G. I. Oxidation of Benzene to Phenol by Nitrous Oxide: Activity of Iron in Zeolite Matrices of Various Composition. *Appl. Catal., A* **2002**, *227*, 143−157.